

# **Turbulence Measurements from Compliant Moorings - Part II: Motion**

## **Correction**

Levi F. Kilcher\*

*National Renewable Energy Laboratory, Golden, Colorado, USA*

Jim Thomson

*Applied Physics Laboratory, University of Washington, Seattle, Washington, USA*

Samuel Harding

*Pacific Northwest National Laboratory, Richland, Washington, USA*

Sven Nylund

*Nortek AS, Norway*

\* *Corresponding author address:* Levi Kilcher, National Renewable Energy Laboratory, 15013 Denver West Pkwy, Golden, Colorado, USA

E-mail: Levi.Kilcher@nrel.gov

## ABSTRACT

14 Acoustic Doppler velocimeters (ADV) are a valuable tool for making  
15 high-precision measurements of turbulence, and moorings are a convenient  
16 and ubiquitous platform for making many kinds of measurements in the  
17 ocean. However, because of concerns that mooring motion can contami-  
18 nate turbulence measurements and acoustic Doppler profilers are relatively  
19 easy to deploy, ADVs are not frequently deployed from moorings. This  
20 work demonstrates that inertial motion measurements can be used to reduce  
21 motion-contamination from moored ADV velocity measurements. Three dis-  
22 tinct mooring platforms were deployed in a tidal channel with inertial-motion-  
23 sensor-equipped ADVs. In each case, the motion correction based on the in-  
24 ertial measurements dramatically reduced contamination from mooring mo-  
25 tion. The spectra from these measurements have a shape that is consistent  
26 with other measurements in tidal channels, and have a  $f^{-5/3}$  slope at high  
27 frequencies—consistent with Kolmogorov’s theory of isotropic turbulence.  
28 Motion correction also improves estimates of cross spectra and Reynold’s  
29 stresses. Comparison of turbulence dissipation with flow speed and turbu-  
30 lence production indicates a bottom boundary layer production-dissipation  
31 balance during ebb and flood that is consistent with the strong tidal forcing  
32 at the site. These results indicate that inertial-motion-sensor-equipped ADVs  
33 are a valuable new tool for measuring turbulence from moorings.

## 34 1. Introduction

35 Acoustic Doppler velocimeters (ADV) have been used to make high-precision measurements of  
36 water velocity for over 20 years (Kraus et al. 1994; Lohrmann et al. 1995). During that time, they  
37 have been deployed around the world to measure turbulence from a range of platforms, including  
38 the laboratory setting (Voulgaris and Trowbridge 1998), from stationary structures on ocean-, river-  
39 and lake-bottoms (Kim et al. 2000; Lorke 2007; Cartwright et al. 2009), in surface waters from  
40 a pole lowered from a ship’s bow (Geyer et al. 2008), and in the deep ocean from autonomous  
41 underwater vehicles (e.g., Zhang et al. 2001; Goodman et al. 2006).

42 A relatively small fraction of ADV measurements have been made from moorings (e.g., Fer  
43 and Paskyabi 2014). Presumably this is because mooring motion can contaminate ADV mea-  
44 surements, and acoustic Doppler profilers (ADPs) can be used to measure mid-depth turbulence  
45 statistics without a mooring (e.g., Stacey et al. 1999a; Rippeth et al. 2002; Wiles et al. 2006).  
46 Still, ADV measurements have distinct characteristics that can be advantageous: they are capa-  
47 ble of higher sample rates, have higher signal-to-noise ratios, and have a much smaller sample  
48 volume (1 centimeter, as opposed to several meters). That is, compared to an ADP, ADVs are  
49 high-precision instruments capable of providing unique information. They could be more widely  
50 used as a moored instrument (i.e., at an arbitrary depth) if a method for accounting for mooring  
51 motion can be demonstrated to provide more accurate estimates of turbulence statistics.

52 Inertial motion unit (IMU) sensors have been used in the aerospace and aeronautical industries  
53 to quantify the motion of a wide range of systems, and to improve atmospheric velocity measure-  
54 ments, for several decades (Axford 1968; Edson et al. 1998; Bevly 2004). Over the last 10 years,  
55 the smartphone, drone, and ‘Internet of Things’ markets have driven innovation in microelectrical-  
56 mechanical systems, including the IMU. As a result of this growth and innovation, the cost, power

57 requirements, and size of IMUs have come down. These changes have allowed these sensors to be  
58 integrated into oceanographic instruments that have small form-factors, and rely on battery power.

59 Nortek now offers a version of their Vector ADV with a Microstrain 3DM-GX3-25 IMU sensor  
60 (Nortek 2005; MicroStrain 2012). This IMU's signals are incorporated into the Vector data stream,  
61 so that its motion and orientation signals are tightly synchronized with the ADV's velocity mea-  
62 surements. This tight synchronization provides a data stream that can be utilized to quantify ADV  
63 motion in the Earth's inertial reference frame, and remove that motion from the ADV's velocity  
64 measurements at each time step of its sampling (Edson et al. 1998). This work utilizes moored  
65 'ADV-IMU' measurements from mid-depths in Puget Sound to demonstrate that motion correc-  
66 tion can improve the accuracy of oceanic turbulence spectra, turbulence dissipation, and Reynolds  
67 stress estimates from moored platforms.

68 This effort was originally motivated by a need for low-cost, high-precision turbulence measure-  
69 ments for the emerging tidal energy industry (McCaffrey et al. 2015; Alexander and Hamlington  
70 2015). Experience in the wind energy industry has shown that wind turbine lifetime is reduced  
71 by atmospheric turbulence, and the same is expected to be true for tidal energy turbines. In the  
72 atmosphere, meteorological towers are often used to position sonic anemometers at the hub height  
73 of wind turbines for measuring detailed turbulence inflow statistics (Hand et al. 2003; Kelley et al.  
74 2005; Mücke et al. 2011; Afgan et al. 2013). In the ocean, tower-mounted hub-height turbulence  
75 measurements have been made, but they are challenging to install and maintain in energetic tidal  
76 sites (Gunawan et al. 2014; Thomson et al. 2012). Therefore, the U.S. Department of Energy  
77 funded this work to investigate the accuracy of mooring-deployed ADV-IMUs to reduce the cost  
78 of turbulence measurements at tidal energy sites (Kilcher et al. 2016). The approach proved to be  
79 successful and potentially useful to the broader oceanographic community interested in moored

80 turbulence measurements (Lueck and Huang 1999; Doherty et al. 1999; Nash et al. 2004; Moum  
81 and Nash 2009; Alford 2010; Paskyabi and Fer 2013).

82 The next section describes details of the measurements, including a summary of the hardware  
83 configurations (platforms) that were used to support and position the ADV-IMUs in the water  
84 column. A detailed description of the motion of these platforms is found in the companion paper to  
85 this work, Harding et al. (in review), hereafter Part 1. Section 3 describes the mathematical details  
86 of motion correction and Section 4 presents results from applying the method to measurements  
87 from the various platforms. Section 5 is a discussion of the energetics of the tidal channel in  
88 which the measurements were made and demonstrates that the measurements are consistent with  
89 turbulence theory and other measurements in similar regimes. A summary and concluding remarks  
90 are provided in Section 6.

## 91 **2. Measurements**

92 This work focuses on measuring turbulence from ADVs that are equipped with IMUs and de-  
93 ployed from moving (moored) platforms. The ADVs utilized for these measurements were Nortek  
94 Vector ADVs equipped with Microstrain 3DM-GX3-25 IMU sensors. These IMUs captured all  
95 six components of the ADV motion (three components of angular rotation and three components  
96 of linear acceleration), as well as the orientation of the ADV pressure case. The sampling of the  
97 motion sensor is tightly synchronized with the ADV measurements. The IMU measures its mo-  
98 tion at 1 kHz and uses internal signal integration (Kalman filtering) to output the motion signals  
99 at the same sample rate as the ADV's velocity measurements. This reduces aliasing of the IMU's  
100 motion measurements above the ADV's sample rate (MicroStrain 2010). Cable-head ADVs were  
101 used throughout this work to allow for flexibility in the positioning of the ADV head relative to its  
102 pressure case.

103 All measurements used in this work were made in Admiralty Inlet, Washington, approximately  
104 500 m west southwest of Admiralty Head in 60 m of water near 48° 9.18' N, 122° 41.22' W (Figure  
105 1). The site is approximately 6 km east of Port Townsend, and 1 km north of the Port Townsend  
106 to Coupeville ferry route. Admiralty inlet is the largest waterway connecting Puget Sound to  
107 the Strait of Juan de Fuca, and it possesses a large semidiurnal tidal flow (Thomson et al. 2012;  
108 Polagye and Thomson 2013). This work utilizes data from three distinct deployment platforms:  
109 the tidal turbulence mooring, a StableMoor buoy, and a simple sounding weight. All data used  
110 in this analysis are available from the MHK data repository (<http://mhkdr.openei.org>; submission  
111 ids: 49, 50 and 51). Each of these platforms are briefly described below, and additional details,  
112 photos, and schematic diagrams can be found in Part 1.

### 113 *a. Tidal Turbulence Mooring*

114 The tidal turbulence mooring (TTM) is a simple mooring system with a strongback fin sus-  
115 pended between a steel clump-weight anchor weighing 1,200 kg when dry and a 0.93-m-diameter  
116 spherical steel buoy with a buoyancy of 320 kg. The ADV pressure cases were clamped to one  
117 side of the strongback fin and the ADV sensor head was positioned 10 cm in front of the fin's  
118 leading edge (Figure 2). The leading edge of the fin is fastened inline with the mooring line. This  
119 configuration was designed to work like a weather vane, such that the drag on the fin held the ADV  
120 head upstream of the mooring components. This work utilizes data from two TTM deployments.

121 The first TTM deployment was in June 2012 from 17:30 on the 12th until 14:30 on the 14th  
122 (local; i.e., Pacific Daylight Time). Two Nortek ADVs were clamped to either side of the fin so that  
123 the axis of their cylindrical pressure cases were parallel with the leading edge of the strongback.  
124 The ADV heads were spaced 0.5 m apart vertically along the fin. Only one of these ADVs was

125 equipped with an integrated IMU. This TTM also had an upward-looking acoustic Doppler profiler  
126 mounted on the mooring anchor.

127 Periods of time during which this mooring interfered with a beam of the Doppler profiler were  
128 identified by inspecting the profiler's acoustic amplitude signal. Periods during which one beam  
129 of the profiler had  $> 5\%$  higher acoustic amplitude than the other beams were flagged as "contam-  
130 inated" and excluded from averaging. Five-minute averages in which more than 50% of the data  
131 were contaminated in this way were masked as invalid.

132 The second TTM deployment was in 2014 from 06:00 on June 17 to 05:00 on June 19 (local  
133 time). Two Nortek ADV-IMUs were mounted on this TTM, with their heads spaced 0.5 m apart  
134 along the fin. In this case, the pressure cases and ADV heads were inclined at an angle of  $18^\circ$  to  
135 the leading edge of the fin to account for mooring blowdown during strong currents (Figure 3).  
136 This change was made to reduce vibrational motion observed during the June 2012 deployment  
137 that was believed to be associated with the orientation of the pressure cases.

#### 138 *b. The StableMoor platform*

139 The second deployment platform was a cylindrical, StableMoor, syntactic foam buoy (manufac-  
140 turer: Deep Water Buoyancy) that was anchored to a clump weight that weighed 1,200 kg (Figure  
141 4). The buoy is 3.5 m long and 0.45 m in diameter with a tail ring that is 0.76 m in diameter. The  
142 StableMoor buoy weighs 295 kg in air, and has a buoyancy of 185 kg in water.

143 The StableMoor buoy was deployed with an ADV-IMU mounted at its nose from 11:21 on May  
144 12 to 11:53 on May 13, 2015 (local time). The sample volume of the ADV is 10 cm forward of  
145 the nose and 20 cm above the center line of the StableMoor buoy (Figure 4). Based on Wyngaard  
146 et al.'s (1985) investigation of a similarly shaped slender body, the velocity measurements should  
147 have flow-distortion effects of less than 10%. This configuration was designed to be the most

148 stable platform for measuring turbulence from a moving platform. The StableMoor buoy was  
149 equipped with a 1,200-kHz RDI workhorse sentinel acoustic Doppler profiler that was oriented  
150 downward-looking to measure water velocity below the platform in twelve 1-m bins and measure  
151 buoy motion (“bottom tracking”), all at a 1-Hz sample rate.

152 The buoy was ballasted to pitch upward a few degrees in zero-flow to avoid “flying downward”.  
153 In the presence of an oncoming current, the tail fins help to orient it into the flow. The anchor for  
154 this buoy is similar to that of the TTM, including an acoustic release so the mooring and anchor  
155 can be recovered separately.

156 The StableMoor platform has two primary advantages compared to the TTM. First, it is signif-  
157 icantly more massive and hydrodynamically stable than the TTM, which reduces the frequency  
158 of motions of the platform. Second, the StableMoor platform is capable of supporting a bottom-  
159 tracking acoustic Doppler profiler, which provides an independent measure of the platform’s trans-  
160 lational motion. Disadvantages of the StableMoor include: its size, which adds to the challenge of  
161 deployment and recovery, and its cost, which is significantly higher than the TTM system.

### 162 *c. Turbulence Torpedo*

163 The turbulence torpedo is a simple sounding weight with an ADV head mounted forward of the  
164 nose, and the ADV pressure case strapped below (Figure 5). This platform was deployed on May  
165 14, 2015, for 37 minutes starting at 07:41 local time. This measurement was made from a davit  
166 that hung the system from the side of the ship to a depth of approximately 25 m. The primary  
167 logistical advantages of this platform are its compact size, low cost, and the flexibility to perform  
168 spatial transects.



169 *d. Coordinate system and turbulence averaging*

170 Unless stated otherwise, vector quantities in this work are in a fixed “principal-axes” coordinate  
 171 system that is aligned with the bidirectional tidal flow: positive  $u$  is in the direction of ebb (310°  
 172 True), positive  $w$  is vertically upward, and  $v$  is the cross-stream component in a right-handed  
 173 coordinate system. The full velocity vector,  $\vec{u} = (\tilde{u}, \tilde{v}, \tilde{w})$ , is separated into a mean and turbulent  
 174 component as  $\vec{u} = \overline{\vec{u}} + \vec{u}'$ , where the over-bar denotes a 5-minute average. Turbulence kinetic  
 175 energy,  $\text{tke} = \overline{u'^2} + \overline{v'^2} + \overline{w'^2}$ , and Reynold’s stresses,  $\overline{uv}$ ,  $\overline{uw}$ ,  $\overline{vw}$ , are computed by averaging over the  
 176 5-minute window. Throughout this work, we use  $\bar{U} = (\bar{u}^2 + \bar{v}^2)^{1/2}$  to denote the mean horizontal  
 177 velocity magnitude.

178 All spectra,  $S\{x\}(f) = |\mathcal{F}\{x(t)\}|^2$ , and cross spectra,  $C\{x, y\}(f) = \text{real}(\mathcal{F}\{x(t)\}\mathcal{F}\{y(t)\})$ , are  
 179 computed using NumPy fast Fourier transform routines (van der Walt et al. 2011). Here,  $\mathcal{F}\{x(t)\}$   
 180 denotes the fast Fourier transform of a signal  $x(t)$ . Time series, e.g.,  $x(t)$ , are linearly detrended  
 181 and Hanning windowed prior to computing  $\mathcal{F}\{x\}$  to reduce spectral reddening.

182 Throughout the remainder of this work, the dependence of  $S$  and  $C$  on  $f$  is implied (e.g.,  $S\{x\}(f)$   
 183 is hereafter  $S\{x\}$ ), and for other variables the dependence on  $t$  is implied. Spectra and cross  
 184 spectra are normalized to preserve variance:  $\int S\{u\}df = \overline{u^2}$ , and  $\int C\{u, v\}df = \overline{uv}$ . The notations  
 185  $S\{\vec{u}\} = (S\{u\}, S\{v\}, S\{w\})$ , and  $C\{\vec{u}\} = (C\{u, v\}, C\{u, w\}, C\{v, w\})$  denote the set of spectra and  
 186 cross spectra for each velocity component and pairs of components, respectively.

187 Turbulence dissipation rates are computed as:

$$\varepsilon = \frac{1}{\bar{U}} \left( \alpha \left\langle (S\{u\} + S\{v\} + S\{w\}) f^{5/3} \right\rangle_{f_{IS}} \right)^{3/2} \quad (1)$$

188 where  $\alpha = 0.5$  and  $\langle \rangle_{f_{IS}}$  denotes an average over the inertial subrange of the velocity spectra and  
 189 where the signal-to-noise ratio is small (Lumley and Terray 1983; Sreenivasan 1995). Throughout

190 this work, we take this average from 0.3 to 1 Hz for the  $u$  and  $v$  components, and 0.3 to 3 Hz for  
 191 the  $w$  component.

### 192 3. Methodology

193 The fundamental approach of this methodology is to take velocity measurements from a moving  
 194 velocity sensor,  $\vec{u}_m$ , and use independent measurements of that sensor's motion,  $\vec{u}_h$ , to remove the  
 195 motion from the velocity measurements and thus estimate the ‘motion corrected velocity’:

$$\vec{u}(t) = \vec{u}_m(t) + \vec{u}_h(t) \quad . \quad (2)$$

196 Note here that the ‘+’-sign is correct because head motion,  $\vec{u}_h$ , induces a measured velocity in  
 197 the opposite direction of the head motion itself ( $\vec{u}_m = \vec{u} - \vec{u}_h$ ). This approach has been used  
 198 to successfully correct sonic anemometer measurements of atmospheric turbulence (e.g., Edson  
 199 et al. 1998; Miller et al. 2008). In the ocean, previous works have utilized inertial motion sensors  
 200 to quantify the motion of multiscale profilers for the purpose of measuring the full spectrum of  
 201 oceanic shear (Winkel et al. 1996).

202 The Microstrain IMU available in the Nortek Vector ADV measures the linear acceleration,  $\vec{a}$ ,  
 203 rotational motion,  $\vec{\omega}$ , and orientation matrix,  $\mathbf{R}$ , of the ADV pressure case (body) in the Earth  
 204 reference frame at every time step of the ADV's sampling. So long as the ADV head is rigidly  
 205 connected to the IMU (i.e. the ADV pressure case), the motion of the ADV head is calculated  
 206 from these signals as the sum of rotational and translational motion:

$$\begin{aligned} \vec{u}_h &= \vec{u}_\omega + \vec{u}_a + \vec{u}_{low} \\ &= \mathbf{R}^T \cdot \vec{\omega}^*(t) \times \vec{\ell}^* + \int \{\vec{a}(t)\}_{HP(f_a)} dt + \vec{u}_{low} \end{aligned} \quad (3)$$

207 Here, \* superscripts denote quantities in the ADV's local coordinate system, and  $\vec{\ell}^*$  is the vec-  
 208 tor from the IMU to the ADV head.  $\mathbf{R}^T$ —the inverse of the orientation matrix—rotates vectors

from the IMU to the Earth reference frame. The notation  $\{\vec{a}\}_{HP(f_a)}$  indicates that the IMU’s accelerometer signal is high-pass filtered (in the Earth’s stationary reference frame) at a chosen filter frequency,  $f_a$ . Without such filtering, low-frequency noise in  $\vec{a}$ —sometimes referred to as bias drift—is amplified by integration to the point that it overwhelms the higher frequency information (Barshan and Durrant-Whyte 1995; Bevy 2004; Gulmammadov 2009).  $\vec{u}_{\text{low}}$  is the low-frequency translational motion that is unresolved by  $\vec{u}_a$ , and it is discussed in more detail below. Note that, to avoid double counting,  $\vec{u}_{\text{low}}$  should be estimated by applying the complementary low-pass filter to the independent measurement of low-frequency motion. We use fourth order, bidirectional (zero-phase), Hanning filters for all filtering operations.

The spectra of  $\vec{u}_a$  and  $\vec{u}_\omega$  from an ADV-IMU resting motionless on a table are instructive in understanding the importance of filtering (Figure 6). Because the IMU is stationary, these spectra indicate the noise levels of each signal. The noise level of  $S\{\vec{u}_\omega\}$  (yellow) is several orders of magnitude lower than the velocity spectra we measured (grey region), and also more than an order of magnitude smaller than the Doppler noise levels of the ADV. Here we have used  $\vec{\ell}^* = 1$  m; which is the order-of-magnitude of the typical distance between the ADV head and the IMU. This indicates that the precision of  $\vec{u}_\omega$  (i.e. the angular rate sensor) is adequate for making corrections to ADV velocity measurements without filtering.

The noise level of  $S\{\vec{u}_a\}$  (Figure 6, black), on the other hand, is dominated by a  $f^{-2}$  slope that results from integrating the low-frequency noise in  $\vec{a}$ . The high-pass filtering reduces this noise so that it does not contaminate motion correction, but any real motion that does exist at these frequencies is lost (Egeland 2014; VanZwieten et al. 2015). This means there is a residual low-frequency translational motion,  $\vec{u}_{\text{low}}$ , that needs to be measured independently—or at the very least considered—when using ADV-IMU data from moving platforms.

For the StableMoor buoy, the ADP bottom-track agrees with  $\vec{u}_a$  over a narrow frequency band (see appendix A1), indicating that the ADP and IMU are resolving the same motion. Furthermore,  $\vec{u}_{low}$  derived from the ADP bottom-track gives a noteworthy improvement in the shape of  $S\{u\}$  and  $S\{v\}$  when compared to similar spectra that assume  $\vec{u}_{low} = 0$ . In the latter case, spectral peaks and dips are present between 0.01 and 0.1 Hz that are inconsistent with other measurements of oceanic turbulence (not shown). This indicates that ADP bottom-track measurements are important for resolving turbulence spectra from the StableMoor buoy platform. For the StableMoor buoy we utilize  $f_a = 0.2\text{Hz}$  (5-s period); further details of this choice can be found in appendix A1.

For the TTM the ADV position, relative to its base, can be estimated by assuming the mooring acts like a rigid pole and using the IMU orientation matrix to estimate the pole's 'lean'. The position obtained from this model can then be differentiated to estimate  $\vec{u}_{low}$  (this model does not apply at high frequencies). Spectra of  $\vec{u}_{low}$  estimated using this approach for the June 2014 TTM deployment (Figure 6, blue) are plotted up to the point where they cross their respective  $S\{\vec{u}_a\}$  noise level (black). Together, these two lines provide an 'aggregate noise level' of translational velocity estimates for the TTM: the rigid pole estimate of  $\vec{u}_{low}$  indicates the amplitude of unresolved motion at low- $f$  (blue), and  $S\{\vec{u}_a\}$  indicates the limits of the IMU at high- $f$  (black). Coincidentally,  $S\{\vec{u}_a\}$  filtered at  $f_a = 0.0333\text{Hz}$  is not a terrible approximation for this aggregate noise level. Furthermore, because this aggregate noise level is more than an order of magnitude lower than the velocity spectra of interest (shaded region), the results of motion correction are essentially identical whether we use the rigid pole model to estimate  $\vec{u}_{low}$ , or if we simply assume that  $\vec{u}_{low} = 0$ . Either way, we use  $f_a = 0.0333\text{Hz}$  (30-s period) for the TTM.

The choice of  $f_a$  for reducing low-frequency accelerometer noise depends on the application of the measurement and the platform being used. In particular, filter selection involves a trade-off

between filtering out the bias drift noise while not filtering out measured motion that is unresolved by an independent measurement of  $\vec{u}_{\text{low}}$ .

Additional details on motion correction—including a detailed accounting of the distinct coordinate systems of the IMU, ADV pressure case, and ADV head—can be found in Kilcher et al. (2016). Open-source Python tools for performing motion correction of ADV-IMU data—including scripts that write processed data in Matlab and tabulated formats—are available at <http://lkilcher.github.io/dolfyn/>.

## 4. Results

### *a. Mean velocity*

Figure 7 shows a comparison of  $\vec{u}$  measured by an ADV-IMU mounted on a TTM, to an upward-looking acoustic Doppler profiler mounted on the TTM anchor. This comparison shows excellent agreement between the ADV and Doppler profiler measurements of mean velocity. The  $\bar{u}$ ,  $\bar{v}$ , and  $\bar{w}$  components have a root-mean-square error of 0.05, 0.13, and 0.03 m/s, respectively. Although it is important to note that there is some discrepancy between ADP- and ADV-measured velocities (especially in  $\bar{v}$ , which is most likely due to incomplete motion correction), the agreement between the magnitude and direction of these independent velocity measurements indicates that moored ADV-IMUs provide a reliable estimate of mean velocity in the Earth’s reference frame.

### *b. TTM spectra*

As discussed in detail in Part 1, the mooring motion of the TTM,  $S\{\vec{u}_h\}$ , has a peak at 0.1 to 0.2 Hz from swaying of the mooring that is most likely driven by eddy shedding from the spherical buoy (Figure 8, red lines). There is also higher-frequency broadband motion that is associated with fluttering of the strongback fin around the mooring line. Both of these motions are especially

energetic in the  $v$ -component spectra because this is the direction in which the TTM mooring system is most unstable. As is expected from fluid-structure interaction theory, the amplitude of these motions increases with increasing mean velocity (Morison et al. 1950).

The mooring motion contaminates the uncorrected ADV measurements of velocity,  $S\{\vec{u}_m\}$ , whenever the amplitude of the motion is similar to or greater than the amplitude of the turbulence. Fortunately, much of this motion can be removed using the IMU's motion signals as detailed in Section 3. Lacking an independent measurement of turbulence velocity at this site, we interpret the agreement of these spectra with turbulence theory as evidence that motion correction has improved the velocity measurements. In particular, at high frequencies ( $f > 0.3$  Hz) for each mean-flow speed, the spectra decay with a  $f^{-5/3}$  slope and have equal amplitude across the velocity components. These results are consistent with Kolmogorov's (1941) theory of isotropic turbulence, and are consistent with spectral shapes of earlier measurements of turbulence in energetic tidal channels from stationary platforms (Walter et al. 2011; Thomson et al. 2012; McMillan et al. 2016).

For  $|\vec{u}| > 1.0$ , motion correction modifies the  $u$  and  $v$  component spectra at frequencies as high as 3 Hz. This outcome indicates that in order for motion correction to be effective, synchronization between the ADV and IMU needs to be within 1/3 s or better. This suggests that asynchronous approaches to motion correction may be challenging, especially considering that the clock drift of some instrumentation can be as high as a few seconds per day. By integrating the IMU data into the ADV data stream, the Nortek ADV-IMU achieves a synchronization to within 1e-2 s.

At low frequencies the spectra tend to become roughly constant (especially at higher flow speeds), which is also consistent with previous works. Note that the very low magnitude of  $S\{\vec{u}_h\}$  at low frequencies is partially a result of filtering the IMU's accelerometer signal when calculating  $\vec{u}_a$ . The true low-frequency spectrum of ADV head motion is unknown (indicated using a dashed

301 line below  $f_a$ ). A comparison of  $S\{\vec{u}\}$  measured by the TTM to that measured by the ADP—during  
302 the June 2012 deployment—reveals agreement at low frequencies (not shown). This finding sug-  
303 gests that the assumption that  $\vec{u}_{\text{low}} = 0$  at these frequencies and at this site for this platform is  
304 justified—even if  $S\{\vec{u}_h\}$  is not as low as indicated in Figure 8.

305 As successful as motion correction is, some of the motion contamination persists in  $S\{\vec{u}\}$ . This  
306 is most notable in  $S\{v\}$  at the highest flow speeds ( $> 2.0$  m/s): a peak at 0.15 Hz is an order of  
307 magnitude larger than a spectral fit to the other frequencies would indicate. This persistent motion  
308 contamination is evident to a lesser degree in  $S\{u\}$  for  $|u| > 2$  m/s, and in  $S\{v\}$  at lower flow  
309 speeds.  $S\{w\}$  appears to have no persistent motion contamination because the amplitude of the  
310 motion in this direction is much lower than for the other two components. For these measurements,  
311  $S\{w_h\}$  is so low that  $w$ -component motion correction makes only a minor correction to the spectra.

312 The amplitude of the persistent motion contamination peaks in  $S\{v\}$  at 0.15 Hz is a factor of 5  
313 to 10 times smaller than the amplitude of the ADV head motion itself. This observation suggests  
314 that the Microstrain IMU can be used to effectively correct mooring motion at 0.15 Hz when  
315 the amplitude of that motion is less than 5 times the amplitude of the real turbulence spectrum.  
316 As a result, we have chosen a value of 3 as a conservative estimate of the motion correction’s  
317 effectiveness.

318 In addition to the primary benefit of correcting for mooring motion, the IMU measurements  
319 can also be used to identify and screen out persistent motion contamination. For example, one  
320 of the most common uses of turbulence spectra is for the calculation of  $\epsilon$  and  $\text{tke}$ . For these  
321 purposes, and based on the relative amplitudes of the 0.15-Hz peaks, we assume that persistent  
322 motion contamination is likely, where  $S\{\vec{u}_h\}/S\{\vec{u}\} > 3$ , and thereby exclude these regions from  
323 spectral fits.

324 In the present case, for the  $u$  and  $w$  spectra, this criteria only excludes a narrow range of frequen-  
 325 cies at the 0.15-Hz motion peak for some cases. This criteria is more restrictive of the  $v$ -component  
 326 spectra at high frequencies for  $\bar{U} > 1.0$  m/s, but this may be acceptable because the amplitude of  
 327  $S\{v\}$  at these frequencies—i.e., in the isotropic inertial subrange—should be equal to that of  $S\{u\}$   
 328 and  $S\{w\}$  (Kolmogorov 1941).

329 Agreement of the  $v$ -component spectral amplitude with that of  $u$  and  $w$  at frequencies  $> 0.3$  Hz  
 330 indicates that motion correction is effective at those frequencies even when  $S\{\vec{u}_h\}/S\{\vec{u}\} \gtrsim 3$ . This  
 331 outcome suggests that our screening threshold is excessively conservative at those frequencies,  
 332 and that a more precise screening threshold may be frequency dependent. For example, it might  
 333 take into account the  $f^3$  character of the noise in  $S\{\vec{u}_a\}$  (Figure 6). For the purpose of this work,  
 334 the  $S\{\vec{u}_h\}/S\{\vec{u}\} < 3$  threshold for spectral fits is sufficient, and detailed characterization of the  
 335 IMU’s motion- and frequency-dependent noise level is left for future work.

### 336 *c. StableMoor Spectra*

337 The spectra of the StableMoor motion has a broader peak with a maximum amplitude that is ap-  
 338 proximately half the frequency of the TTM spectral peak (Figure 9). The motion of this platform  
 339 also does not have high-frequency “subpeaks” or other high-frequency broadbanded excitation  
 340 (Part 1). These characteristics of the motion are most likely due to the more massive and hydro-  
 341 dynamically streamlined properties of the platform.

342 Like the TTM, the motion-corrected spectra from the StableMoor buoy are consistent with turbu-  
 343 lence theory and previous observations. Most importantly, there is an improvement in the quality  
 344 of the motion-corrected spectra compared to the TTM. In particular, the persistent motion con-  
 345 tamination peaks are completely removed. That is, this measurement system provides an accurate



346 estimate of the turbulence spectra at this location from low frequencies to more than 1 Hz—well  
347 into the inertial subrange—for all three components of velocity.

348 Note that this level of accuracy cannot be obtained without the independent estimate of  $\vec{u}_{\text{low}}$ .  
349 If we assume that  $\vec{u}_{\text{low}} = 0$ , a similar plot to Figure 9 (not shown) reveals persistent motion-  
350 contamination peaks and troughs in the  $u$  and  $v$  spectra regardless of the choice of  $f_a$ . This as-  
351 sumption indicates that the low-frequency motion of the StableMoor buoy is below a threshold in  
352 which the IMU’s signal-to-noise ratio is high enough to resolve its motion. In other words, com-  
353 pared to the TTM, the StableMoor platform provides a more accurate measurement of turbulence  
354 when it includes an independent measure of  $\vec{u}_{\text{low}}$  (here a bottom-tracking ADCP), but it does no  
355 better—and perhaps worse—when it does not.

#### 356 *d. Torpedo spectra*

357 The  $u$  and  $v$  motion of the turbulence torpedo is broadband and the  $w$  motion has a narrow peak  
358 at 0.3 Hz (Figure 10). Because  $\vec{u}_h$  is estimated using  $f_a = 0.0333 \text{ Hz}$  and assuming  $\vec{u}_{\text{low}} = 0$ , its  
359 spectra rolls off quickly below  $f_a$ . Motion correction of the torpedo data appears to effectively re-  
360 move a motion peak from  $S\{w\}$  at 0.3 Hz, and straightens out  $S\{v\}$  between 0.04 and 0.6 Hz.  $S\{u\}$   
361 is mostly unaffected by motion at these frequencies, because the torpedo motion is smaller than  
362 the turbulence in this direction. At frequencies below  $f_a$ ,  $S\{u\}$  and  $S\{v\}$  increase dramatically.  
363 This increase suggests that unresolved, low-frequency motion of the torpedo is contaminating the  
364 velocity measurements at these frequencies. It may be possible to correct for some of this con-  
365 tamination using a measurement of the ship’s motion as a proxy for the torpedo’s low-frequency  
366 motion, but this has not been done. Still, above  $f_a$ , the torpedo appears to provide a reliable  
367 estimate of spectral amplitude in the inertial subrange and can therefore be used to estimate  $\varepsilon$ .  
368 Considering the simplicity of the platform, it may be a useful option for quantifying this turbu-

369 lence statistic in a variety of scenarios. Further, if a GPS is positioned above it, it may be capable  
370 of providing even more.

#### 371 *e. Cross Spectra*

372 Inspection of cross spectra from TTM measurements demonstrates that motion correction can  
373 reduce motion contamination to produce reliable estimates of velocity cross spectra (Figure 11).  
374 At low flow speeds (left column), cross spectra between components of  $\vec{u}_h$  (i.e., between compo-  
375 nents of head motion, red) are small compared to correlated velocities. As the velocity magnitude  
376 increases (center and right columns), the swaying motion of the TTM at 0.15 Hz appears as a peak  
377 in the amplitude of the cross spectra of  $\vec{u}_h$  (red) and  $\vec{u}_m$  (black) for all three components of cross  
378 spectra (rows). Fortunately, motion correction reduces the amplitude of this peak dramatically so  
379 that  $C\{\vec{u}\}$  (blue) is small at 0.15 Hz compared to lower frequencies. Furthermore, the fact that the  
380 standard deviation of  $C\{\vec{u}\}$  is also relatively small at 0.15 Hz suggests that motion correction is  
381 effective for each spectral window, not just in their mean.

382 These results indicate that motion-corrected TTM velocity measurements can be used to obtain  
383 reliable estimates of turbulence Reynold's stresses, which are the integral of the cross spectra.  
384 Without motion correction, Reynold's stress estimates would be contaminated by the large peaks  
385 in the cross spectra that are caused by the swaying and fluttering motion of the TTM vane.

386 A similar investigation of StableMoor cross spectra (not shown) indicates that cross-spectral  
387 motion contamination is at a much lower amplitude than for the TTM. The low-frequency ( $< 0.3$   
388 Hz) "swimming" motion of that platform produces a minimal cross-spectral signal, and the relative  
389 large mass of the platform minimizes the kinds of higher-frequency swaying and fluttering that  
390 creates large values of cross-spectral head motion. Thus, the StableMoor platform also produces  
391 reliable estimates of Reynold's stresses, which are presumed to be improved by motion correction.

## 5. Discussion

The previous section presented a comparison of  $\vec{u}$  measured by a TTM-mounted ADV to measurements from a co-located ADP. This comparison demonstrated that the IMU provides a reliable estimate of the ADV's orientation and that this can be utilized to estimate mean velocity in the Earth's reference frame. Turbulence velocity estimates from the same ADP are also in agreement with low-frequency TTM turbulence estimates (not shown), but the ADP does not resolve turbulence at the scales where motion contamination is strongest (0.1 to 1.0 Hz).

Ideally, moored motion-corrected turbulence velocity measurements would be validated against simultaneous independent validated measurements of turbulence velocity at the same scales and exact time and location. Accomplishing this, however, involves significant technical challenges that are not easily overcome—most notably the difficulty of measuring turbulence at the same point as the moving ADV. A slightly less ideal but much more realistic confirmation of the methodology might involve comparing the statistics of moored turbulence measurements to those from a nearby fixed platform, or a fixed platform placed at the same location at a different time (e.g., the “TTT” platform described in Thomson et al. 2012). Unfortunately, to our knowledge, these measurements have not yet been made.

Lacking a relevant, fixed, independent turbulence measurement to compare to it is instructive to demonstrate the degree to which the moored measurements are consistent with turbulence theory and other turbulence measurements in similar flow environments. The previous section showed that the shape of the turbulence velocity spectra from moored ADVs is consistent with Kolmogorov's theory of locally isotropic turbulence, which has been observed consistently in turbulence measurements for decades (Kolmogorov 1941; Grant et al. 1962; McMillan et al. 2016). In particular, we observed an isotropic subrange—an  $f^{-5/3}$  spectral slope and equal amplitude

spectra between components—that is driven by anisotropic turbulence at longer timescales (Figures 8, 9, 10). This finding is interpreted as the first indication that the measurement systems presented are capable of accurately resolving turbulence. The degree to which uncorrected spectra were corrected toward this theoretical and observationally confirmed shape is interpreted as a measure of the improvement of the spectral estimates by motion correction.

Figure 12 presents a time series of the mean velocity (A) and several turbulence statistics that were measured during the June 2014 TTM deployment. This figure shows the evolution of the flow through Admiralty Inlet during 1.5 tidal cycles. The tke (B), Reynold’s stresses (C), dissipation, and one component of turbulence production (D) grow and strengthen with ebb or flood then subside during slack tide. This component of turbulence production is:

$$P_{uz} = \frac{\partial \bar{u}}{\partial z} \overline{uw} \quad . \quad (4)$$

Where  $\partial \bar{u} / \partial z$  is computed from the two ADVs on the TTM. The highest values of  $\varepsilon$  and  $P_{uz}$  occur at the peak of the ebb or flood, which is in agreement with other measurements in tidal channels. The agreement of the magnitude of  $P_{uz}$  with  $\varepsilon$  at those times suggests a local production-dissipation balance that is often observed in tidally forced channels (Trowbridge et al. 1999; Stacey et al. 1999b; McMillan et al. 2016). At other times, the value of  $P_{uz}$  is insufficient to balance  $\varepsilon$  or is negative.

Inspection of the negative  $P_{uz}$  values reveals that most of them are caused by a reversed sign of  $\overline{uw}$  rather than a reversed sign of  $\partial u / \partial z$  (i.e., when compared to the sign of  $u$ ). This finding suggests that uncertainty in  $\overline{uw}$  may be contributing to discrepancies between  $P_{uz}$  and  $\varepsilon$ . Furthermore, considering the complex nature of the shoreline near this site (i.e., the headland), it is not surprising that  $P_{uz}$  does not balance  $\varepsilon$  perfectly. Other terms of the tke equation are likely to be important, such as other components of production, advection terms, or turbulent transport terms. The fact

437 that these two terms are in near balance as often as they are is a strong indication that bottom  
438 boundary layer physics are important to the dynamics at this site.

439 Figure 13 compares individual values of  $P_{uz}$  with  $\varepsilon$  directly. Given the assumptions implicit in  
440 this comparison and the discussion above, the agreement between  $P_{uz}$  and  $\varepsilon$  is an encouraging  
441 result that suggests the turbulent boundary layer reaches the depth of these measurements (10  
442 m) during the highest flow speeds. This result is further supported by a comparison of  $\bar{U}$  with  
443  $\varepsilon$  (Figure 14). Here we see a  $\varepsilon \propto \bar{U}^3$  dependence that is again suggestive of bottom boundary  
444 layer physics (Trowbridge 1992; Nash et al. 2009). At lower flow speeds,  $\varepsilon$  deviates from this  
445 relationship, which suggests that the boundary layer is no longer the dominant physical process at  
446 the depth of these measurements.

## 447 6. Conclusion

448 This work presents a methodology for measuring turbulence from moored ADV-IMUs and  
449 demonstrates that motion correction reduces mooring motion-contamination. Comparison of spec-  
450 tra of ADV head motion,  $S\{\vec{u}_h\}$ , to that of motion-corrected,  $S\{\vec{u}\}$ , and uncorrected spectra,  
451  $S\{\vec{u}_m\}$ , reveals that motion correction improves spectral estimates of moored ADV measurements.  
452 In particular, we found that motion-corrected spectra have spectral shapes that are similar to previ-  
453 ous measurements of tidal-channel turbulence and have a  $f^{-5/3}$  spectral slope at high frequencies.  
454 This finding suggests that the motion-corrected spectra resolve the inertial subrange predicted by  
455 Kolmogorov’s theory of locally isotropic turbulence.

456 Motion correction reduces motion contamination for all platforms we presented but it does not  
457 necessarily remove it completely. This outcome seems to depend on the relative amplitude of  
458 platform motion compared to the underlying turbulence being measured. The most notable ex-  
459 ample of this is from the TTM, which has a large “swaying” peak at 0.1 Hz. Where this peak

460 is very large—especially in the  $v$  component—it is not reduced to a level that is consistent with  
461 earlier measurements of tidal-channel turbulence—i.e., there is no smooth roll-off between the  
462 low-frequency energy-containing scales and the  $f^{-5/3}$  inertial subrange.

463 This inconsistency indicates that turbulence measurements from moored, motion-corrected  
464 ADV-IMUs must be interpreted with care. An inspection of spectra presented here suggests that  
465 excluding spectral regions where  $S\{\vec{u}_h\}/S\{\vec{u}\} > 3$  removes persistent-motion contamination peaks  
466 while still preserving spectral regions where motion correction is effective. Using this criteria, it  
467 is then possible to produce spectral fits that exclude persistent-motion contamination, and provide  
468 reliable estimates of turbulence quantities of interest (e.g.,  $\varepsilon$  and  $\text{tke}$ ).

469 We have also shown that motion correction reduces motion contamination in cross spectra. This  
470 finding is important because it suggests that moored ADV-IMU measurements may be used to  
471 produce reliable estimates of Reynolds stresses. We utilized these stress estimates and vertical  
472 shear estimates, both from the TTM, to estimate  $P_{uz}$ .

473 Finally, we have shown that  $\varepsilon$  estimates based on motion-corrected spectra scale with the  $U^3$ , and  
474 balance  $P_{uz}$  estimates during ebb and flood. Together, these results indicate that bottom boundary  
475 layer physics are a dominant process at this site, and that the boundary layer reaches the height  
476 of the ADV-IMUs (10 m) during ebb and flood. The degree of agreement between  $P_{uz}$  and  $\varepsilon$  also  
477 serves as an indicator of the self-consistency of moored ADV-IMU turbulence measurements.

478 *Acknowledgments.* Many thanks to Joe Talbert, Alex DeKlerk, Captain Andy Reay-Ellers, Jen-  
479 nifer Rinker, Maricarmen Guerra, and Eric Nelson in assisting with data collection. The authors  
480 are also grateful to James VanZwieten, Matthew Egeland and Marshall Richmond for discussion  
481 on the details of this work.

482 Thanks to the open-source software community for the tools used in this work, especially the  
483 developers of L<sup>A</sup>T<sub>E</sub>X, Python, NumPy, Matplotlib, git, and GNU emacs.

484 This work was supported by the U.S. Department of Energy under Contract No. DE-AC36-  
485 08GO28308 with the National Renewable Energy Laboratory. Funding for the work was provided  
486 by the DOE Office of Energy Efficiency and Renewable Energy, Wind and Water Power Technolo-  
487 gies Office.

488 The U.S. Government retains and the publisher, by accepting the article for publication, ac-  
489 knowledges that the U.S. Government retains a nonexclusive, paid-up, irrevocable, worldwide  
490 license to publish or reproduce the published form of this work, or allow others to do so, for U.S.  
491 Government purposes.

## A1. Comparing StableMoor $\vec{u}_{\text{low}}$ to IMU $\vec{u}_{\text{h}}$

To better understand the IMU’s signal-to-noise ratio, we compare the motion of the StableMoor buoy from the ADP bottom track measurements,  $\vec{u}_{\text{BT}}$ , to the IMU’s estimates of ADP motion. To do this, we compute the IMU’s estimate of ADP motion using equation (3), and replacing  $\ell^*$  with the vector that points from the IMU to the ADP head. In this case, we use a 5 minute high-pass filter ( $f_a = 0.00333$ ) in (3); this reduces spectral reddening that otherwise contaminates coherence estimates and preserves the  $\vec{u}_a$  estimates at the frequencies where we wish to compare to  $\vec{u}_{\text{BT}}$  (Figure 15). We also linearly interpolate the ADP measurements of  $\vec{u}_{\text{BT}}$  onto the times of the ADV-IMU measurements.

The coherence between these two signals is high and statistically significant over 1.5 decades—from 0.03 to 0.8 Hz (Figure 15, Priestley 1981). The  $v$  component has the highest coherence, 98%, because this is the direction that has the most motion (i.e., these estimates have a higher signal-to-noise ratio). The  $u$  and  $w$  components have a slightly lower coherence, 80% and 65%, respectively.

On the low-frequency side, our interpretation is that the signal-to-noise ratio of the IMU decreases dramatically below 0.03 Hz, resulting in low coherence. On the high-frequency side, Doppler noise in the ADP measurements contaminates its estimates of motion, causing the decrease in coherence at 0.8 Hz. A comparison of the phase between these signals shows that there is no lag between the measurements (not shown).

These results help to inform the selection of zero-lag filters used to estimate  $\vec{u}_{\text{low}}$  from  $\vec{u}_{\text{BT}}$ . In particular, by selecting 0.2 Hz, we target the middle of the coherence peak between the two measurements. Furthermore, the rapid decrease in coherence below 0.03 Hz provides an objective



515 measurement of the frequency at which IMU measured velocity becomes unreliable in the flow  
516 conditions we observed.

## 517 **References**

518 Afgan, I., J. McNaughton, S. Rolfo, D. Apsley, T. Stallard, and P. Stansby, 2013: Turbulent flow  
519 and loading on a tidal stream turbine by les and rans. *International Journal of Heat and Fluid*  
520 *Flow*, **43**, 96–108.

521 Alexander, S. R., and P. E. Hamlington, 2015: Analysis of turbulent bending moments in tidal  
522 current boundary layers. *Journal of Renewable and Sustainable Energy*, **7 (6)**, 063 118.

523 Alford, M. H., 2010: Sustained, full-water-column observations of internal waves and mixing near  
524 mendocino escarpment. *Journal of Physical Oceanography*, **40 (12)**, 2643–2660, doi:10.1175/  
525 2010JPO4502.1.

526 Axford, D., 1968: On the accuracy of wind measurements using an inertial platform in an aircraft,  
527 and an example of a measurement of the vertical mesostructure of the atmosphere. *Journal of*  
528 *Applied Meteorology*, **7 (4)**, 645–666.

529 Barshan, B., and H. F. Durrant-Whyte, 1995: Inertial navigation systems for mobile robots. *IEEE*  
530 *Transactions on Robotics and Automation*, **11 (3)**, 328–342.

531 Bevly, D. M., 2004: Global positioning system (gps): A low-cost velocity sensor for correcting in-  
532 ertial sensor errors on ground vehicles. *Journal of dynamic systems, measurement, and control*,  
533 **126 (2)**, 255–264.

534 Cartwright, G. M., C. T. Friedrichs, P. J. Dickhudt, T. Gass, and F. H. Farmer, 2009: Using the  
535 acoustic doppler velocimeter (adv) in the mudbed real-time observing system. *Marine Technol-*  
536 *ogy for Our Future: Global and Local Challenges*.

537 Doherty, K., D. Frye, S. Liberatore, and J. Toole, 1999: A moored profiling instrument\*. *Journal*  
538 *of Atmospheric and Oceanic Technology*, **16** (11), 1816–1829.

539 Edson, J. B., A. A. Hinton, K. E. Prada, J. E. Hare, and C. W. Fairall, 1998: Direct covariance  
540 flux estimates from mobile platforms at sea\*. *Journal of Atmospheric and Oceanic Technology*,  
541 **15** (2), 547–562, doi:10.1175/1520-0426(1998)015<0547:DCFEFM>2.0.CO;2.

542 Egeland, M. N., 2014: Spectral evaluation of motion compensated ADV systems for ocean turbu-  
543 lence measurements. Ph.D. thesis, Florida Atlantic University.

544 Fer, I., and M. B. Paskyabi, 2014: Autonomous ocean turbulence measurements using shear probes  
545 on a moored instrument. *Journal of Atmospheric and Oceanic Technology*, **31** (2), 474–490, doi:  
546 10.1175/JTECH-D-13-00096.1.

547 Finlayson, D., 2005: Combined bathymetry and topography of the Puget Lowlands, Washington  
548 state. URL <http://www.ocean.washington.edu/data/pugetsound/>.

549 Geyer, R. W., M. E. Scully, and D. K. Ralston, 2008: Quantifying vertical mixing in estuaries.  
550 *Environmental Fluid Mechanics*, **8**, 495–509, doi:10.1007/s10652-008-9107-2.

551 Goodman, L., E. R. Levine, and R. G. Lueck, 2006: On measuring the terms of the turbulent  
552 kinetic energy budget from an auv. *Journal of Atmospheric and Oceanic Technology*, **23** (7),  
553 977–990, doi:10.1175/JTECH1889.1.

554 Grant, H. L., R. W. Stewart, and A. Moilliet, 1962: Turbulence spectra from a tidal channel.  
555 *Journal of Fluid Mechanics*, **12**, 241–263.

556 Gulmammadov, F., 2009: Analysis, modeling and compensation of bias drift in mems inertial  
557 sensors. *Recent Advances in Space Technologies, 2009. RAST'09. 4th International Conference*  
558 *on*, IEEE, 591–596.

559 Gunawan, B., V. S. Neary, and J. Colby, 2014: Tidal energy site resource assessment in the East  
 560 River tidal strait, near Roosevelt Island, New York, NY (USA). *Renewable Energy*, **71**, 509–  
 561 517, doi:10.1016/j.renene.2014.06.002.

562 Hand, M. M., N. D. Kelley, and M. J. Balas, 2003: Identification of wind turbine response to  
 563 turbulent inflow structures. Tech. Rep. NREL/CP-500-33465, National Renewable Energy Lab-  
 564 oratory.

565 Harding, S., L. Kilcher, and J. Thomson, 2017: Turbulence measurements from compliant moor-  
 566 ings - part 1: Motion characterization, in review.

567 Kelley, N. D., B. J. Jonkman, G. N. Scott, J. T. Bialasiewicz, and L. S. Redmond, 2005: The impact  
 568 of coherent turbulence on wind turbine aeroelastic response and its simulation. *WindPower*,  
 569 Denver, Colorado, NREL/CP-500-38074, may 15-18.

570 Kilcher, L., J. Thomson, J. Talbert, and A. DeKlerk, 2016: Measuring turbulence from moored  
 571 acoustic Doppler velocimeters: A manual to quantifying inflow at tidal energy sites. 9 62979,  
 572 National Renewable Energy Laboratory. URL [www.nrel.gov/docs/fy16osti/62979.pdf](http://www.nrel.gov/docs/fy16osti/62979.pdf).

573 Kim, S. C., C. T. Friedrichs, J. P.-Y. Maa, and L. D. Wright, 2000: Estimating bottom stress in  
 574 tidal boundary layer from acoustic doppler velocimeter data. *Journal of Hydraulic Engineering*,  
 575 399–406.

576 Kolmogorov, A. N., 1941: Dissipation of energy in the locally isotropic turbulence. *Dokl. Akad.*  
 577 *Nauk SSSR*, **32** (1), 16–18, URL <http://www.jstor.org/stable/51981>.

578 Kraus, C., A. Lohrmann, and R. Cabrera, 1994: A new acoustic meter for measuring 3d laboratory  
 579 flows. *Journal of Hydraulic Engineering*, **120**, 406–412.

580 Lohrmann, A., R. Cabrera, G. Gelfenbaum, and J. Haines, 1995: Direct measurements of reynolds  
581 stress with an acoustic doppler velocimeter. *Current Measurement, 1995., Proceedings of the*  
582 *IEEE Fifth Working Conference on*, 205–210, doi:10.1109/CCM.1995.516175.

583 Lorke, A., 2007: Boundary mixing in the thermocline of a large lake. *Journal of Geophysical*  
584 *Research: Oceans*, **112 (C9)**, n/a–n/a, doi:10.1029/2006JC004008, c09019.

585 Lueck, R. G., and D. Huang, 1999: Dissipation measurement with a moored instrument in a swift  
586 tidal channel. *Journal of atmospheric and oceanic technology*, **16**, 1499–1505.

587 Lumley, J., and E. Terray, 1983: Kinematics of turbulence convected by a random wave field.  
588 *Journal of Physical Oceanography*, **13 (11)**, 2000–2007.

589 McCaffrey, K., B. Fox-Kemper, P. E. Hamlington, and J. Thomson, 2015: Characterization of  
590 turbulence anisotropy, coherence, and intermittency at a prospective tidal energy site: Observa-  
591 tional data analysis. *Renewable Energy*, **76**, 441–453.

592 McMillan, J. M., A. E. Hay, R. G. Lueck, and F. Wolk, 2016: Rates of dissipation of turbulent  
593 kinetic energy in a high reynolds number tidal channel. *Journal of Atmospheric and Oceanic*  
594 *Technology*, **33 (4)**, 817–837, doi:10.1175/JTECH-D-15-0167.1.

595 MicroStrain, I., 2010: Technical note: Coning and sculling. Tech. Rep. I0019, MicroStrain. URL  
596 [http://files.microstrain.com/TN-I0019\\_3DM-GX3-25\\_\\_Coning\\_And\\_Sculling.pdf](http://files.microstrain.com/TN-I0019_3DM-GX3-25__Coning_And_Sculling.pdf).

597 MicroStrain, I., 2012: *3DM-GX3-15,-25 MIP Data Communications Protocol*. URL [http:](http://files.microstrain.com/3DM-GX3-15-25-MIP-Data-Communications-Protocol.pdf)  
598 [//files.microstrain.com/3DM-GX3-15-25-MIP-Data-Communications-Protocol.pdf](http://files.microstrain.com/3DM-GX3-15-25-MIP-Data-Communications-Protocol.pdf), retrieved  
599 January 2014.

600 Miller, S. D., T. S. Hristov, J. B. Edson, and C. A. Friehe, 2008: Platform motion effects on  
 601 measurements of turbulence and air-sea exchange over the open ocean. *Journal of Atmospheric  
 602 and Oceanic Technology*, **25 (9)**, 1683–1694, doi:10.1175/2008JTECHO547.1.

603 Morison, J. R., J. W. Johnson, and S. A. Schaaf, 1950: The force exerted by surface waves on  
 604 piles. *Journal of Petroleum Technology*, **2 (05)**, 149–154.

605 Moum, J., and J. Nash, 2009: Mixing measurements on an equatorial ocean mooring. *Journal of  
 606 Atmospheric and Oceanic Technology*, **26 (2)**, 317–336.

607 Mücke, T., D. Kleinhans, and J. Peinke, 2011: Atmospheric turbulence and its influence on the  
 608 alternating loads on wind turbines. *Wind Energy*, **14**, 301–316.

609 Nash, J. D., L. F. Kilcher, and J. N. Moum, 2009: Structure and composition of a strongly  
 610 stratified, tidally pulsed river plume. *Journal of Geophysical Research*, **114**, C00B12, doi:  
 611 10.1029/2008JC005036.

612 Nash, J. D., E. Kunze, J. M. Toole, and R. W. Schmitt, 2004: Internal tide reflection and turbulent  
 613 mixing on the continental slope. *Journal of Physical Oceanography*, **34 (5)**, 1117–1134, doi:  
 614 10.1175/1520-0485(2004)034<1117:ITRATM>2.0.CO;2.

615 Nortek, 2005: *Vector Current Meter User Manual*. Vangkroken 2, NO-1351 RUD, Norway, h ed.

616 Paskyabi, M. B., and I. Fer, 2013: Turbulence measurements in shallow water from a subsurface  
 617 moored moving platform. *Energy Procedia*, **35**, 307 – 316, doi:10.1016/j.egypro.2013.07.183.

618 Polagye, B., and J. Thomson, 2013: Tidal energy resource characterization: methodology and field  
 619 study in admiralty inlet, Puget Sound, WA (USA). *Proceedings of the Institution of Mechanical  
 620 Engineers, Part A: Journal of Power and Energy*, **227 (3)**, 352–367.

621 Priestley, M., 1981: *Spectral Analysis and Time Series*. Academic Press, London.

622 Rippeth, T. P., E. Williams, and J. H. Simpson, 2002: Reynolds stress and turbulent en-  
623 ergy production in a tidal channel. *Journal of Physical Oceanography*, **32**, 1242–1251, doi:  
624 10.1175/1520-0485(2002)032\$(\$1242:RSATEP\$)\$2.0.CO;2.

625 Sreenivasan, K. R., 1995: On the universality of the Kolmogorov constant. *Physics of Fluids*, **7**,  
626 2778–2784.

627 Stacey, M. T., S. G. Monismith, and J. R. Burau, 1999a: Measurements of reynolds stress  
628 profiles in unstratified tidal flow. *J. Geophys. Res.*, **104 (C5)**, 10 933–10 949, doi:10.1029/  
629 1998JC900095.

630 Stacey, M. T., S. G. Monismith, and J. R. Burau, 1999b: Observations of turbulence in a partially  
631 stratified estuary. *Journal of Physical Oceanography*, **29**, 1950–1970.

632 Thomson, J., B. Polagye, V. Durgesh, and M. Richmond, 2012: Measurements of turbulence at  
633 two tidal energy sites in Puget Sound, WA. *Journal of Oceanic Engineering*, **37 (3)**, 363–374,  
634 doi:10.1109/JOE.2012.2191656.

635 Trowbridge, J. H., 1992: A simple description of the deepening and structure of a stably stratified  
636 flow driven by a surface stress. *Journal of Geophysical Research*, **97**, 15 529–15 543.

637 Trowbridge, J. H., W. R. Geyer, M. M. Bowen, and A. J. I. Williams, 1999: Near-bottom turbu-  
638 lence measurements in a partially mixed estuary: turbulent energy balance, velocity structure  
639 and along-channel momentum balance. *Journal of Physical Oceanography*, **29**, 3056–3072.

640 van der Walt, S., S. C. Colbert, and G. Varoquaux, 2011: The numpy array: A structure for efficient  
641 numerical computation. *Computing in Science & Engineering*, **13**, 22–30, doi:10.1109/MCSE.  
642 2011.37.

643 VanZwieten, J. H., M. N. Egeland, K. D. von Ellenrieder, J. W. Lovenbury, and L. Kilcher, 2015:  
 644 Experimental evaluation of motion compensated adv measurements for in-stream hydrokinetic  
 645 applications. *Current, Waves and Turbulence Measurement (CWTM)*, 2015 IEEE/OES Eleventh,  
 646 1–8, doi:10.1109/CWTM.2015.7098119.

647 Voulgaris, G., and J. H. Trowbridge, 1998: Evaluation of the acoustic doppler velocimeter (adv)  
 648 for turbulence measurements. *Journal of Atmospheric and Oceanic technology*, **15**, 272–289.

649 Walter, R. K., N. J. Nidzieko, and S. G. Monismith, 2011: Similarity scaling of turbulence spectra  
 650 and cospectra in a shallow tidal flow. *Journal of Geophysical Research: Oceans*, **116** (C10).

651 Wiles, P. J., T. P. Rippeth, J. H. Simpson, and P. J. Hendricks, 2006: A novel technique for  
 652 measuring the rate of turbulent dissipation in the marine environment. *Geophysical Research*  
 653 *Letters*, **33**, 21 608.

654 Winkel, D., M. Gregg, and T. Sanford, 1996: Resolving oceanic shear and velocity with the multi-  
 655 scale profiler. *Journal of Atmospheric and Oceanic Technology*, **13** (5), 1046–1072.

656 Wyngaard, J. C., L. Rockwell, and C. A. Friehe, 1985: Errors in the measurement of turbulence  
 657 upstream of an axisymmetric body. *Journal of Atmospheric and Oceanic Technology*, **2** (4),  
 658 605–614.

659 Zhang, Y., K. Streitlien, J. G. Bellingham, and A. B. Baggeroer, 2001: Acoustic doppler ve-  
 660 locimeter flow measurement from an autonomous underwater vehicle with applications to deep  
 661 ocean convection. *Journal of Atmospheric and Oceanic Technology*, **18** (12), 2038–2051, doi:  
 662 10.1175/1520-0426(2001)018<2038:ADVFMF>2.0.CO;2.

## LIST OF FIGURES

<b>Fig. 1.</b>	Bathymetry of Admiralty Inlet near Port Townsend, Washington, U.S.A. (Finlayson 2005). The red dot indicates the location of all measurements. The positive $u$ direction is the direction of ebb flow (thick arrow originating from red dot), and positive $v$ is away from Admiralty Head (smaller arrow).	34
<b>Fig. 2.</b>	Schematic diagram of the TTM; not to scale.	35
<b>Fig. 3.</b>	TTM components on the deck of the R/V Jack Robertson. The TTM includes two ADVs, with pressure cases mounted on opposite sides of the fin. The anchor stack includes a pop-up buoy for retrieval. The green arrow indicates the vector from the IMU to the ADV head (face of the transmit transducer).	36
<b>Fig. 4.</b>	Top: Alex DeKlerk checks to ensure that the StableMoor buoy is properly fastened to its anchor; the RDI workhorse ADCP can be seen in the rear instrument bay. A bridle is draped across the top of the buoy for deployment and recovery, and a small marker buoy fastened to the tail is useful during recovery. Bottom: a close-up of the StableMoor buoy with the ADV head and the top of its pressure case. The green arrow indicates the vector from the IMU to the ADV head.	37
<b>Fig. 5.</b>	The turbulence platform showing details of the ADV head and pressure case configuration. The green arrow indicates the vector from the IMU to the ADV head. The head cable was taped out of the way beneath the sounding weight tail fins shortly after taking this photo.	38
<b>Fig. 6.</b>	Spectra of $\vec{u}_\omega$ (yellow) and $\vec{u}_a$ signals from the Microstrain IMU sitting on a motionless table. The $\vec{u}_a$ signals are unfiltered (black), and high-pass filtered at 30 s (magenta) and 5 s (green). Vertical dotted lines indicate the filter frequency. Blue lines are an estimate of $\vec{u}_{low}$ for the TTM. Solid lines are the horizontal components, and dashed lines are the vertical components of $\vec{u}_a$ and $\vec{u}_{low}$ . The horizontal and vertical Doppler noise levels of a Nortek Vector ADV configured to measure $\pm 4\text{m/s}$ are indicated by horizontal dash-dot and dotted lines, respectively. The shaded region indicates the range of $u$ spectral amplitudes presented herein ( $0.002 < \text{tke} < 0.03 \text{ m}^2/\text{s}^2$ , $1\text{e-}5 < \varepsilon < 5\text{e-}4 \text{ W/kg}$ ).	39
<b>Fig. 7.</b>	Time series of tidal velocity at Admiralty Head from ADV-IMU measurements (black), and an acoustic Doppler profiler on the anchor (red). The profiler measurements—taken at the same depth as the ADV on the TTM—were contaminated by acoustic reflection from the strongback fin when it was inline with one of the profiler’s beams. Note that the vertical scale on the three axes vary by more than an order of magnitude; the small ticks in A and B are equivalent to the ticks in C.	40
<b>Fig. 8.</b>	Turbulence spectra from the June 2014 TTM deployment. Each column is for a range of streamwise velocity magnitudes (indicated at top). The rows are for each component of velocity (indicated to the lower right of the right column). The uncorrected spectra are in black and the corrected spectra are blue, and the spectra of ADV head motion, $\vec{u}_h$ , is red (also indicated in the legend). The vertical red dotted line indicates the filter frequency applied to the IMU accelerometers when estimating $\vec{u}_h$ ; below this frequency $S\{\vec{u}_h\}$ is plotted as a dashed line. Diagonal black dotted lines indicate a $f^{-5/3}$ slope. The number of spectral ensembles, $N$ , in each column is indicated in the top row.	41
<b>Fig. 9.</b>	Turbulence spectra from the StableMoor buoy. The axes layout and annotations are identical to Figure 8, except that $S\{\vec{u}_h\}$ is plotted as a solid line at all frequencies because it is measured at all frequencies.	42



707	<b>Fig. 10.</b>	Turbulence spectra from the turbulence torpedo during a 35-minute period when the mean velocity was 1.3 m/s. Annotations and line colors are identical to Figure 8. . . . .	43
708			
709	<b>Fig. 11.</b>	The real part of the cross-spectral density between velocity components measured by the TTM. The upper row is the $u$ - $v$ cross-spectral density, the middle row is the $u$ - $w$ cross-spectral density, and the bottom row is the $v$ - $w$ cross-spectral density. The columns are for different ranges of the stream-wise mean velocity magnitude (indicated above the top row). The blue line is the cross spectrum between components of motion-corrected velocity, the red line is the cross spectrum between components of head motion, and the black line is the cross spectrum between components of uncorrected velocity. The light blue shading indicates one standard deviation of the $C$ for the motion-corrected cross-spectral density. $N$ is the number of spectral ensembles in each column. The number in the lower-right corner of each panel is the motion-corrected Reynold's stress (integral of the blue line) in units of $1\text{e-4 m}^2\text{s}^{-2}$ . . . . .	44
710			
711			
712			
713			
714			
715			
716			
717			
718			
719			
720	<b>Fig. 12.</b>	Time series of mean velocities (A), turbulence energy and its components (B), Reynold's stresses (C), and turbulence dissipation rate (D) measured by the TTM during the June 2014 deployment. Shading indicates periods of ebb ( $\bar{u} > 1.0$ , grey) and flood ( $\bar{u} < -1.0$ , lighter grey). . . . .	45
721			
722			
723			
724	<b>Fig. 13.</b>	$P_{u\bar{z}}$ vs. $\varepsilon$ during the June 2014 TTM deployment for values of $ u  > 1$ m/s. Values of negative production are indicated as open circles. . . . .	46
725			
726	<b>Fig. 14.</b>	A log-log plot of $\varepsilon$ vs. $\bar{U}$ for the June 2014 TTM (diamonds) and May 2015 StableMoor (dots) deployments, during ebb (left) and flood (right). Black points are 5-minute averages. Green dots are mean values within speed bins of $0.2 \text{ m s}^{-1}$ width that have at least 10 points (50 minutes of data); their vertical bars are 95% bootstrap confidence intervals. The blue line shows a $U^3$ slope, wherein the proportionality constant (blue box) is calculated by taking the log-space mean of $\varepsilon/U^3$ . . . . .	47
727			
728			
729			
730			
731			
732	<b>Fig. 15.</b>	Coherence between IMU-measured motion of StableMoor buoy and ADP bottom-track velocity for $1.0 < \bar{U} < 1.5$ . The horizontal dashed line indicates the 95% confidence level for the 102 spectral windows in this estimate. The vertical dotted line indicates the frequency of the high-pass filter applied to the IMU accelerometers in estimating $\vec{u}_h$ . . . . .	48
733			
734			
735			

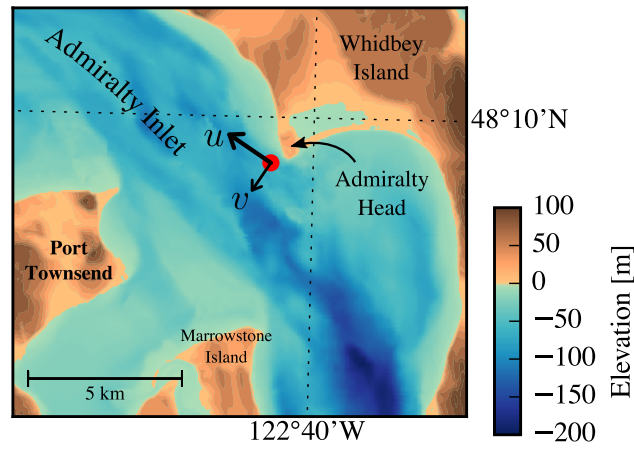


FIG. 1. Bathymetry of Admiralty Inlet near Port Townsend, Washington, U.S.A. (Finlayson 2005). The red dot indicates the location of all measurements. The positive  $u$  direction is the direction of ebb flow (thick arrow originating from red dot), and positive  $v$  is away from Admiralty Head (smaller arrow).

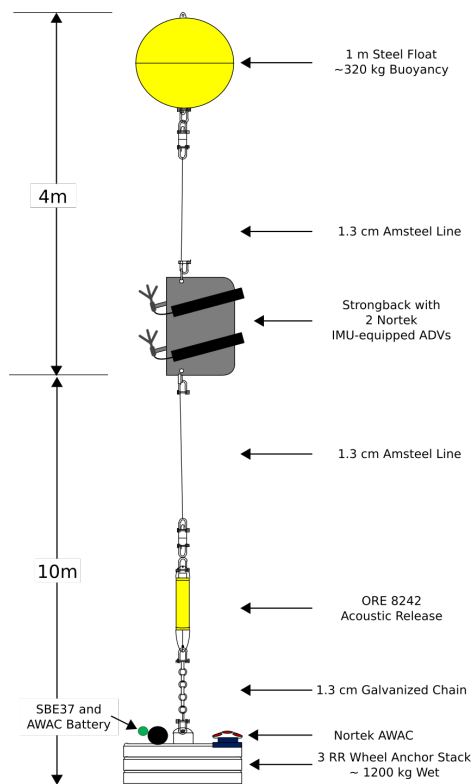


FIG. 2. Schematic diagram of the TTM; not to scale.



739 FIG. 3. TTM components on the deck of the R/V Jack Robertson. The TTM includes two ADVs, with  
 740 pressure cases mounted on opposite sides of the fin. The anchor stack includes a pop-up buoy for retrieval. The  
 741 green arrow indicates the vector from the IMU to the ADV head (face of the transmit transducer).



742 FIG. 4. Top: Alex DeKlerk checks to ensure that the StableMoor buoy is properly fastened to its anchor; the  
 743 RDI workhorse ADCP can be seen in the rear instrument bay. A bridle is draped across the top of the buoy  
 744 for deployment and recovery, and a small marker buoy fastened to the tail is useful during recovery. Bottom: a  
 745 close-up of the StableMoor buoy with the ADV head and the top of its pressure case. The green arrow indicates  
 746 the vector from the IMU to the ADV head.



747 FIG. 5. The turbulence platform showing details of the ADV head and pressure case configuration. The green  
748 arrow indicates the vector from the IMU to the ADV head. The head cable was taped out of the way beneath the  
749 sounding weight tail fins shortly after taking this photo.

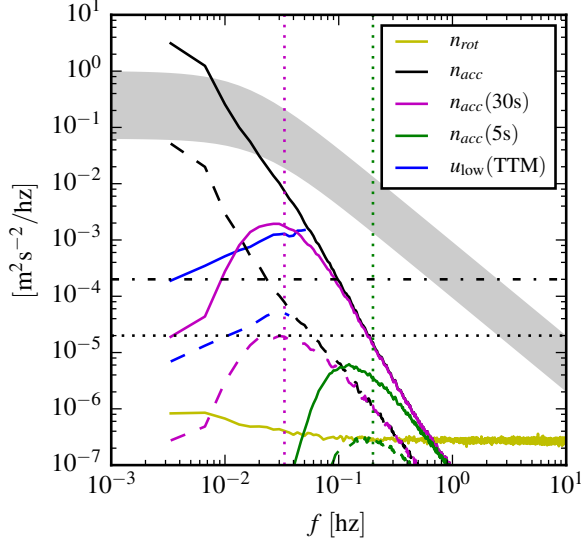
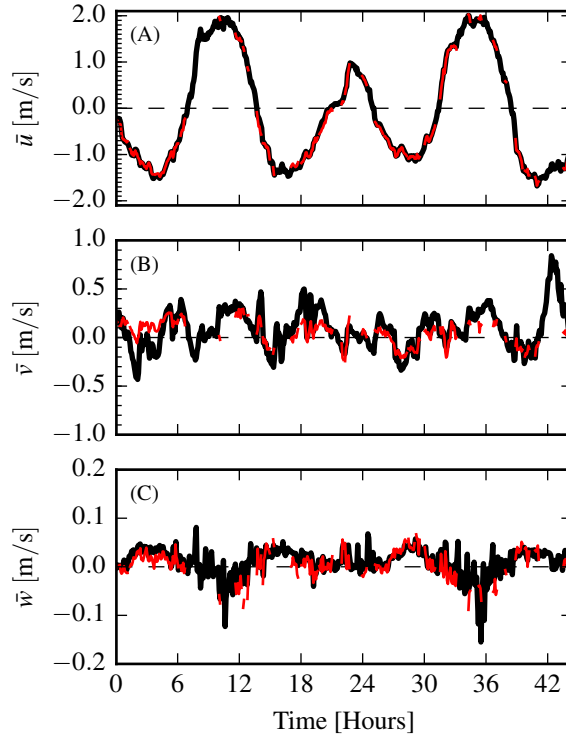


FIG. 6. Spectra of  $\vec{u}_\omega$  (yellow) and  $\vec{u}_a$  signals from the Microstrain IMU sitting on a motionless table. The  $\vec{u}_a$  signals are unfiltered (black), and high-pass filtered at 30 s (magenta) and 5 s (green). Vertical dotted lines indicate the filter frequency. Blue lines are an estimate of  $\vec{u}_{\text{low}}$  for the TTM. Solid lines are the horizontal components, and dashed lines are the vertical components of  $\vec{u}_a$  and  $\vec{u}_{\text{low}}$ . The horizontal and vertical Doppler noise levels of a Nortek Vector ADV configured to measure  $\pm 4\text{m/s}$  are indicated by horizontal dash-dot and dotted lines, respectively. The shaded region indicates the range of  $u$  spectral amplitudes presented herein ( $0.002 < \text{tke} < 0.03 \text{ m}^2/\text{s}^2$ ,  $1\text{e-}5 < \varepsilon < 5\text{e-}4 \text{ W/kg}$ ).



757 FIG. 7. Time series of tidal velocity at Admiralty Head from ADV-IMU measurements (black), and an acoustic  
 758 Doppler profiler on the anchor (red). The profiler measurements—taken at the same depth as the ADV on the  
 759 TTM—were contaminated by acoustic reflection from the strongback fin when it was inline with one of the  
 760 profiler's beams. Note that the vertical scale on the three axes vary by more than an order of magnitude; the  
 761 small ticks in A and B are equivalent to the ticks in C.



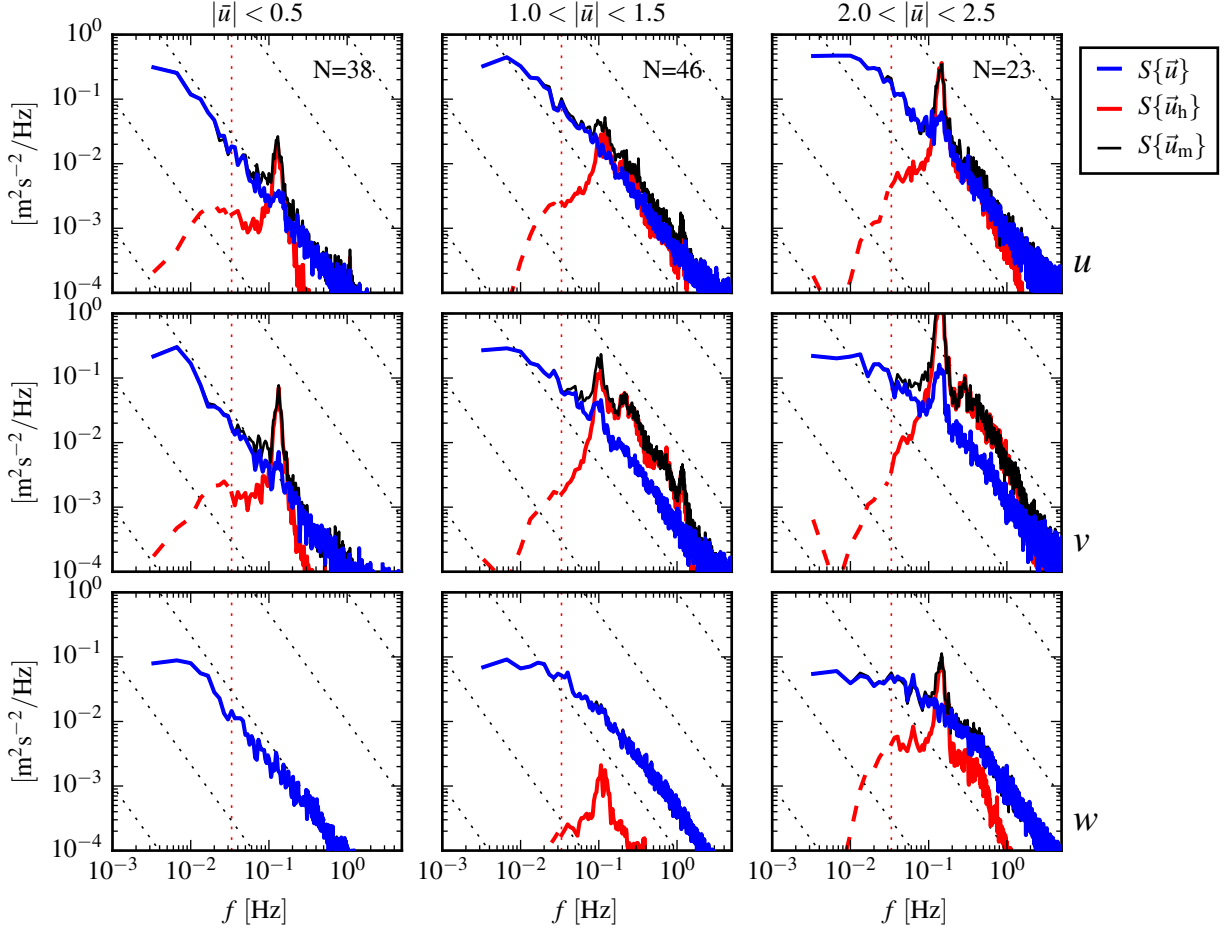


FIG. 8. Turbulence spectra from the June 2014 TTM deployment. Each column is for a range of streamwise velocity magnitudes (indicated at top). The rows are for each component of velocity (indicated to the lower right of the right column). The uncorrected spectra are in black and the corrected spectra are blue, and the spectra of ADV head motion,  $\vec{u}_h$ , is red (also indicated in the legend). The vertical red dotted line indicates the filter frequency applied to the IMU accelerometers when estimating  $\vec{u}_h$ ; below this frequency  $S\{\vec{u}_h\}$  is plotted as a dashed line. Diagonal black dotted lines indicate a  $f^{-5/3}$  slope. The number of spectral ensembles,  $N$ , in each column is indicated in the top row.

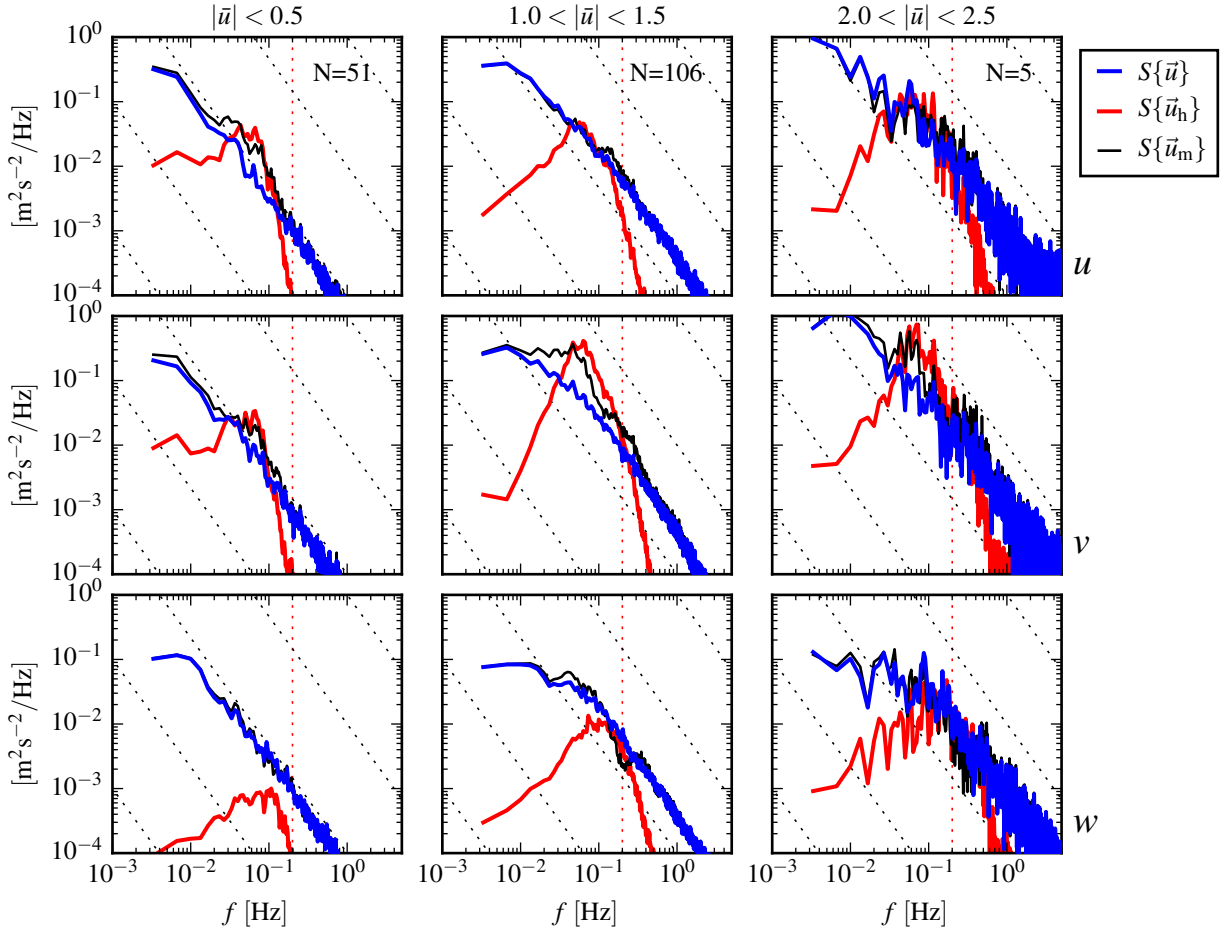
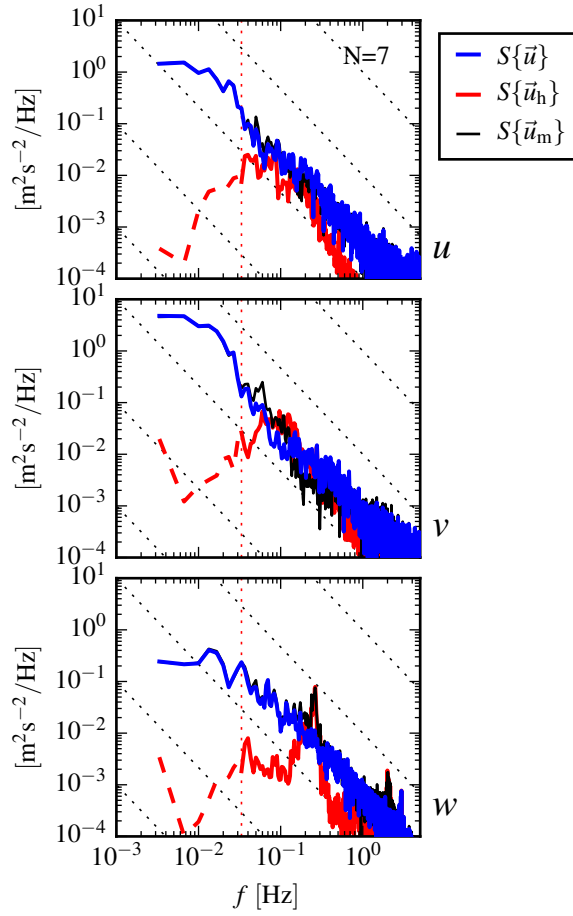


FIG. 9. Turbulence spectra from the StableMoor buoy. The axes layout and annotations are identical to Figure 8, except that  $S\{\vec{u}_h\}$  is plotted as a solid line at all frequencies because it is measured at all frequencies.



771 FIG. 10. Turbulence spectra from the turbulence torpedo during a 35-minute period when the mean velocity  
 772 was 1.3 m/s. Annotations and line colors are identical to Figure 8.

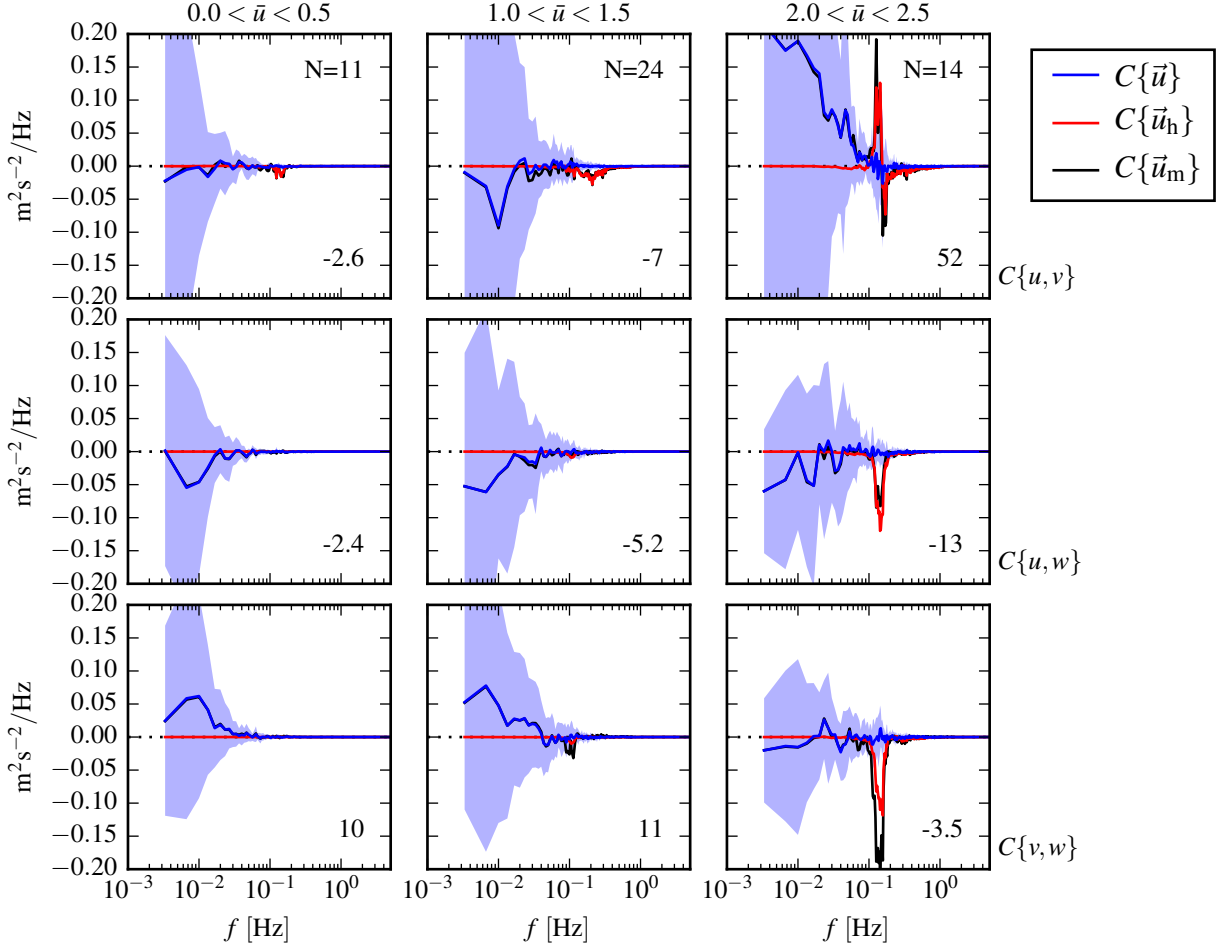


FIG. 11. The real part of the cross-spectral density between velocity components measured by the TTM. The upper row is the  $u$ - $v$  cross-spectral density, the middle row is the  $u$ - $w$  cross-spectral density, and the bottom row is the  $v$ - $w$  cross-spectral density. The columns are for different ranges of the stream-wise mean velocity magnitude (indicated above the top row). The blue line is the cross spectrum between components of motion-corrected velocity, the red line is the cross spectrum between components of head motion, and the black line is the cross spectrum between components of uncorrected velocity. The light blue shading indicates one standard deviation of the  $C$  for the motion-corrected cross-spectral density.  $N$  is the number of spectral ensembles in each column. The number in the lower-right corner of each panel is the motion-corrected Reynold's stress (integral of the blue line) in units of  $1\text{e-}4 \text{ m}^2\text{s}^{-2}$ .

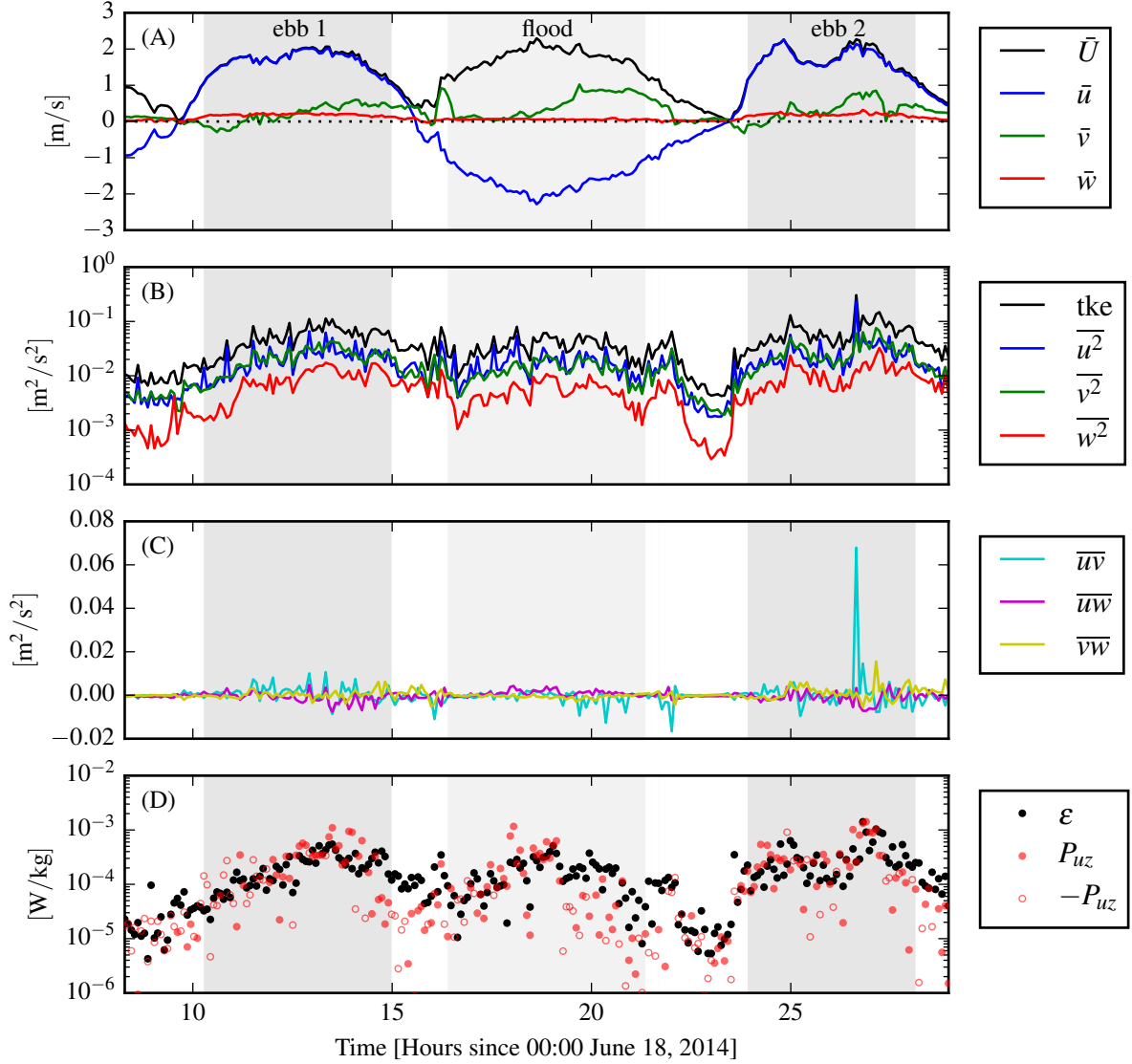
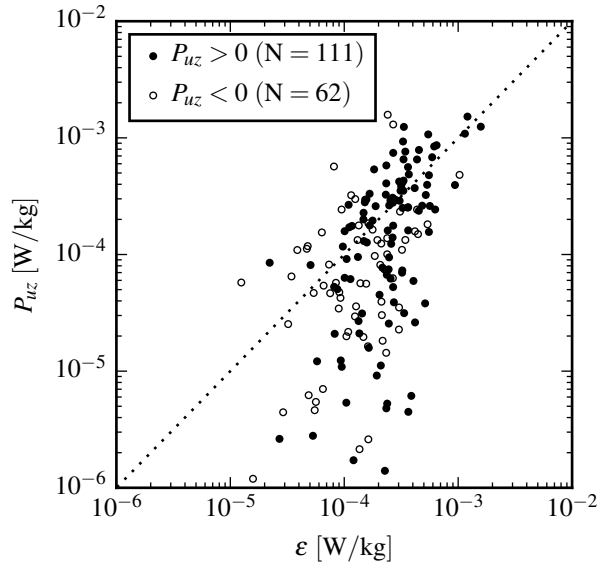


FIG. 12. Time series of mean velocities (A), turbulence energy and its components (B), Reynold's stresses (C), and turbulence dissipation rate (D) measured by the TTM during the June 2014 deployment. Shading indicates periods of ebb ( $\bar{u} > 1.0$ , grey) and flood ( $\bar{u} < -1.0$ , lighter grey).



785 FIG. 13.  $P_{uz}$  vs.  $\varepsilon$  during the June 2014 TTM deployment for values of  $|u| > 1$  m/s. Values of negative  
786 production are indicated as open circles.

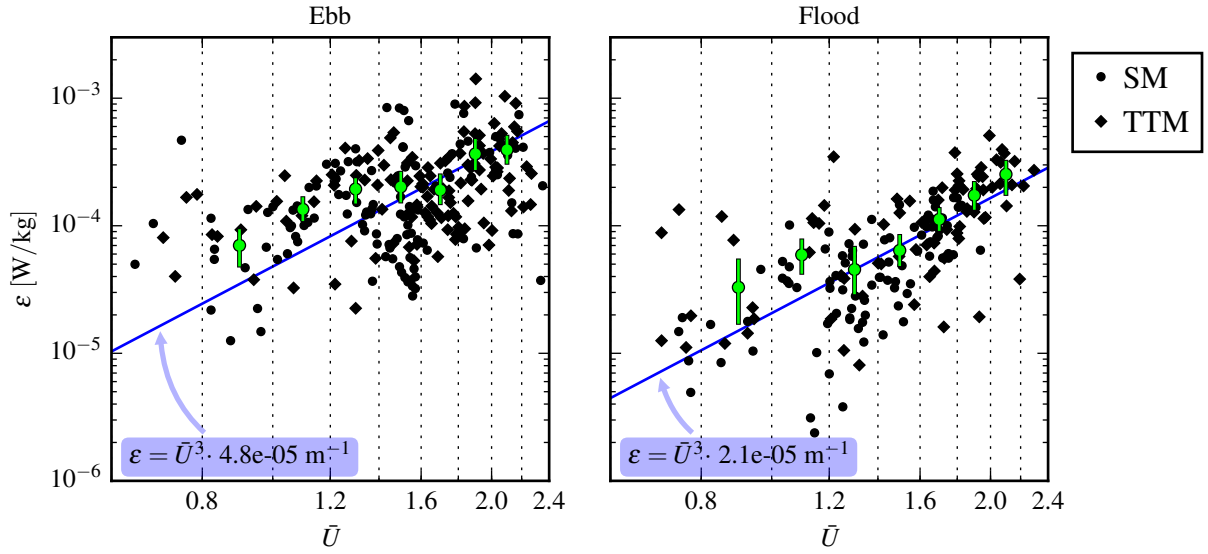


FIG. 14. A log-log plot of  $\epsilon$  vs.  $\bar{U}$  for the June 2014 TTM (diamonds) and May 2015 StableMoor (dots) deployments, during ebb (left) and flood (right). Black points are 5-minute averages. Green dots are mean values within speed bins of  $0.2 \text{ m s}^{-1}$  width that have at least 10 points (50 minutes of data); their vertical bars are 95% bootstrap confidence intervals. The blue line shows a  $U^3$  slope, wherein the proportionality constant (blue box) is calculated by taking the log-space mean of  $\epsilon/U^3$ .

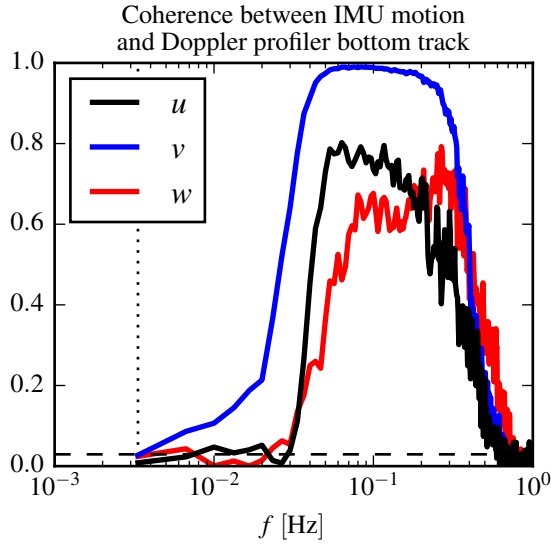


FIG. 15. Coherence between IMU-measured motion of StableMoor buoy and ADP bottom-track velocity for  $1.0 < \bar{U} < 1.5$ . The horizontal dashed line indicates the 95% confidence level for the 102 spectral windows in this estimate. The vertical dotted line indicates the frequency of the high-pass filter applied to the IMU accelerometers in estimating  $\vec{u}_h$ .